

Article

Design and Experiment of a Multi-DOF Shaker Based on Rotationally Symmetric Stewart Platforms with an Insensitive Condition Number

Chao Liang , Weipeng Li, Hai Huang and Yan Zheng *

School of Astronautics, Beihang University, 37 Xueyuan Road, Beijing 100191, China; thomasimagine@buaa.edu.cn (C.L.); liweipeng@buaa.edu.cn (W.L.); hhuang@buaa.edu.cn (H.H.)

* Correspondence: zhengyansa@buaa.edu.cn

Abstract: This study proposes a method for designing a class of rotationally symmetric Stewart platforms (RSSPs) with an insensitive condition number (ICN), which is used to minimize the condition number to achieve a high accuracy for a multi-degree-of-freedom (multi-DOF) shaker. Considering the rotational symmetry of RSSPs, an analytical relationship between the architecture parameters and transfer coefficients is first established. Then, the decoupling conditions of the RSSPs are derived, and the transfer coefficient formulas are simplified by the given decoupling conditions and iso-length assumption. Following further analyses and discussions, the ICN condition and analytical form of the condition number are provided. The area of the ICN (AICN) is, subsequently, derived to evaluate the insensitivity of the condition number. To validate the effectiveness of the method, a design example (ICN-RSSP), along with a numerical analysis, is implemented, and, finally, a multi-DOF shaker is developed. The results of the numerical analysis show a smaller condition number and a larger AICN than those of the RSSP, for comparison. And the experiment results of the multi-DOF shaker show a high accuracy of vibration waveform reproduction. The method can reduce the condition number of RSSPs, improve the insensitivity, and further improve the accuracy of the multi-DOF shaker.

Keywords: rotationally symmetric Stewart platform; condition number; accuracy; decoupling; multi-DOF shaker; parallel mechanism



Citation: Liang, C.; Li, W.; Huang, H.; Zheng, Y. Design and Experiment of a Multi-DOF Shaker Based on Rotationally Symmetric Stewart Platforms with an Insensitive Condition Number. *Actuators* **2023**, *12*, 368. <https://doi.org/10.3390/act12100368>

Academic Editor: André Preumont

Received: 22 August 2023

Revised: 14 September 2023

Accepted: 21 September 2023

Published: 25 September 2023



Copyright: © 2023 by the authors. Licensee MDPI, Basel, Switzerland. This article is an open access article distributed under the terms and conditions of the Creative Commons Attribution (CC BY) license (<https://creativecommons.org/licenses/by/4.0/>).

1. Introduction

Precise payloads of flying vehicles, such as inertial measurement units, gyroscopes, and photoelectric pods, are among the high-sensitive devices used for navigation, transportation, and detection [1–3]. However, the vibration from the carrying platforms, such as the aeroelastic vibration of flying vehicles, reduces the measurement accuracy, reliability, and service life [4,5]. Therefore, vibration tests on these payloads are required for calibration and functional verification [6,7]. These tests are implemented by a single-degree-of-freedom (single-DOF) shaker and are repeated along each sensitive axis of precise payloads to simulate the true multi-DOF vibration environment, including TX, TY, TZ, RX, RY, and RZ [8,9]. As the superposition of the responses by the single-DOF vibration cannot be equivalent to the ones by the multi-DOF vibration [10,11], repeated single-DOF vibration tests can be inaccurate. When the vibration is sufficiently high, nonlinear responses and complex multi-DOF vibration modes can occur [12]. Therefore, the need for multi-DOF vibration tests is reinforced. A multi-DOF shaker is a device used for implementing multi-DOF vibration tests and is based on spatial parallel mechanisms with struts configured as an orthogonal architecture [13] or a Stewart platform architecture [14]. The orthogonal architecture was utilized at first, whereas the Stewart platform was gradually adopted for its smaller area occupation, lower power consumption, higher structural stability, and larger load capacity [15].

Accuracy is a kernel issue for parallel mechanisms [16] because the multi-joint structure of struts can amplify the motion errors of the actuators mounted on the struts [17,18]. The condition number (CN) of the Jacobian matrix [19] is used to describe the error amplification factor, where the Jacobian matrix is utilized to quantify the motion and force transmissibility of the actuators to the mobile plate (MP). A large CN can lead to large errors in the MP or control failure, even if the errors in the actuators are small [20].

To ensure motion accuracy, the CN is often supposed to be minimized during the design of Stewart platforms. Design methods can be divided into numerical and analytical methods. Numerical methods are commonly employed to obtain a smaller CN because the analytical form of the CN cannot be acquired as a function of the architecture parameters [19]. Considering this, Pittens et al. [21] carried out the optimal design of a standard Stewart platform (SSP) and concluded that the minimum CN of the SSP is $\sqrt{2}$. To obtain a smaller CN, Mehta et al. [22] used a generalized Stewart platform (GSP) and obtained a smaller value (1.20). The GSP has a loose design constraint so that it is easier to minimize the CN. However, the lengths of the six struts of the GSP are usually unequal, which leads to the design inconsistency of the actuators and complicates the structure and controller design. In addition, Peng et al. [23] adopted a rotationally symmetric Stewart platform (RSSP) to minimize the CN, which is a typical type of GSP with rotational symmetry and has the benefit of the consistency of the strut lengths.

Compared with the numerical method, the analytical method does not require a large amount of calculation and has a higher design efficiency [24]. Although the relationship between the CN and the architecture parameters of Stewart platforms cannot be directly established, several studies investigated the analytical methods by adding proper constraint conditions. Klein et al. [25] reported that the minimum CN was 1 and that the equivalent constraint condition was isotropic. Yi et al. [26] derived the constraint condition of the architecture parameters when the isotropy was satisfied, but it was too harsh to be directly applied to practical designs [27]. To relax the constraint condition for isotropy, a homogeneous form of the Jacobian matrix was obtained by introducing the characteristic length, and the isotropy can be partly satisfied [28,29]. The aforementioned studies are based on the condition that the manipulation center [30,31] (C_P) is fixed. C_P is the origin of the payload coordinate system {P}, which is a virtual point fixed to the payload and is used to describe the 6-DOF motion of the payload. For a multi-DOF shaker, the C_P is the point at which a vibrational excitation force is applied. In practice, C_P should be changed when referring to different payloads, because the excitation force should coincide with the origin of the sensitive axes [32] of the payload to avoid a measurement error of the angular rate induced by the linear vibration [6,33]. However, this movement causes the CN to increase and further amplify the motion error of the MP [34].

This study proposes an analytic method to design a class of RSSPs, which possesses an “insensitive CN (ICN)” and allows C_P to move in a designable area. This method was subsequently used to design a multi-DOF shaker to maintain the advantages of a high accuracy and applicability to different payloads. By offering the condition of the ICN (ICN condition), the analytical form of the CN can be obtained as a function of the architecture parameters, which improves the efficiency of the design process for minimizing the CN. Meanwhile, the ICN condition is looser than the isotropy condition, making it easier to use in a practical design. The RSSP was selected because it can achieve a smaller CN than the SSP and avoid strut inconsistency in the GSP.

To investigate how CN changes with C_P , the transfer coefficients of the RSSP and the decoupling problem are first investigated. After simplification, the ICN condition is deduced, and the analytical forms of the CN and insensitive domain are provided. Subsequently, a design example (ICN-RSSP) and numerical analysis are conducted to verify the effectiveness of the method at maintaining the CN constant in a larger space of C_P and reducing the errors in the MP. Finally, a multi-DOF shaker is developed based on the ICN-RSSP, and the experiment results are provided. The main contributions of this study are summarized as follows:

- i. The ICN condition is provided, improving the insensitivity of the CN and decreasing the error amplification of the RSSPs when C_p moves in larger space;
- ii. The analytical form of the CN is given by involving the ICN condition, which makes it possible to minimizing the CN by an analytical method and improves the design efficiency and effectiveness;
- iii. A multi-DOF shaker is developed, and the experimental results indicate that the multi-DOF shaker designed using the method is effective for high-accuracy vibration waveform reproduction.

2. Mathematical Foundation

2.1. Problem Description

An RSSP comprises an MP for installing precise payloads, a base plate (BP), and six struts (each strut includes an actuator) connecting the two plates with six upper (p_1, p_2, \dots, p_6) and six lower (b_1, b_2, \dots, b_6) joints (Figure 1). For rotational symmetry [35], the struts were partitioned into two groups: the first group included struts 1, 3, and 5, and the second group contained struts 2, 4, and 6, which were obtained by rotating struts 1 and 2. Hence, the RSSP architecture can be described by the parameters of struts 1 and 2 as follows:

- i. MP radius: r_{p1}, r_{p2} ;
- ii. BP radius: r_{b1}, r_{b2} ;
- iii. Upper-joint distribution angle: ω_{p1}, ω_{p2} ;
- iv. Lower-joint distribution angle: ω_{b1}, ω_{b2} ;
- v. Architecture height: h .

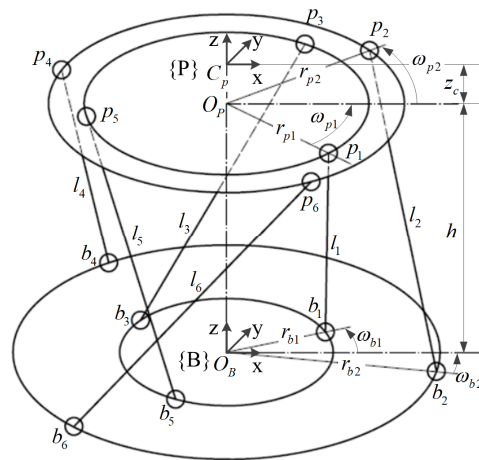


Figure 1. Architecture of RSSP.

The C_p coordinate with reference to the MP center, O_p , is $(x_c, y_c, z_c)^T$, to establish the payload frame {P} for the RSSP with the manipulation center, C_p , as the origin and the base frame {B} with the origin, O_B , at the BP center. To avoid asymmetry, both the {P} and {B} Z axes coincide with the RSSP symmetry axis. And let C_p move along the Z axis, and the coordinate is $(0, 0, z_c)^T$.

Let L be the elongation vector of the six struts and X_p be the displacement vector of the MP (C_p). The transmission between the actuation velocity vector \dot{L} and the velocity vector $\dot{X}_p = (v_{TX}, v_{TY}, v_{TZ}, \omega_{RX}, \omega_{RY}, \omega_{RZ})^T$ can be expressed as

$$\dot{L} = J\dot{X}_p, \tag{1}$$

where \mathbf{J} is the Jacobian matrix

$$\mathbf{J} = \begin{bmatrix} \mathbf{s}_1^T & (\mathbf{p}_1 \times \mathbf{s}_1)^T \\ \vdots & \vdots \\ \mathbf{s}_6^T & (\mathbf{p}_6 \times \mathbf{s}_6)^T \end{bmatrix}, \tag{2}$$

where \mathbf{s}_i is the unit direction vector along the i -th strut; \mathbf{p}_i is the vector pointing to the i -th upper joint p_i , with respect to C_P ; and $i = 1, 2, \dots, 6$.

For struts 1 and 2, we obtain

$$\begin{cases} \mathbf{s}_i = (\sin \theta_i \cos \varphi_i, \sin \theta_i \sin \varphi_i, \cos \theta_i)^T, i = 1, 2 \\ \mathbf{p}_i = (r_{pi} \cos \omega_{pi}, r_{pi} \sin \omega_{pi}, p_{zi})^T, i = 1, 2 \end{cases} \tag{3}$$

where θ_i shows the angle between \mathbf{s}_i and the positive Z axis, and φ_i stands for the angle between the projection of \mathbf{s}_i on the XY plane and positive X axis.

By rotational symmetry, the struts in each group were repeated every $2\pi/3$. Thus, for the other struts, we obtain

$$\begin{aligned} \mathbf{s}_3 &= \mathbf{R}_{z, \frac{2}{3}\pi} \mathbf{s}_1, & \mathbf{p}_3 &= \mathbf{R}_{z, \frac{2}{3}\pi} \mathbf{p}_1, & \mathbf{s}_5 &= \mathbf{R}_{z, \frac{4}{3}\pi} \mathbf{s}_1, & \mathbf{p}_5 &= \mathbf{R}_{z, \frac{4}{3}\pi} \mathbf{p}_1, \\ \mathbf{s}_4 &= \mathbf{R}_{z, \frac{2}{3}\pi} \mathbf{s}_2, & \mathbf{p}_4 &= \mathbf{R}_{z, \frac{2}{3}\pi} \mathbf{p}_2, & \mathbf{s}_6 &= \mathbf{R}_{z, \frac{4}{3}\pi} \mathbf{s}_2, & \mathbf{p}_6 &= \mathbf{R}_{z, \frac{4}{3}\pi} \mathbf{p}_2, \end{aligned} \tag{4}$$

where the rotation matrix is

$$\mathbf{R}_{z, \vartheta} = \begin{bmatrix} \cos \vartheta & -\sin \vartheta & \\ \sin \vartheta & \cos \vartheta & \\ & & 1 \end{bmatrix}, \tag{5}$$

where ϑ is the angle of rotation.

As expressed in Equation (6), the CN is equivalent to the amplification factor [19] of the relative errors in $\dot{\mathbf{L}}$ and $\dot{\mathbf{X}}_P$:

$$\frac{\|\Delta \dot{\mathbf{X}}_P\|}{\|\dot{\mathbf{X}}_P\|} \leq \|\mathbf{J}\| \|\mathbf{J}^{-1}\| \frac{\|\Delta \dot{\mathbf{L}}\|}{\|\dot{\mathbf{L}}\|}, \tag{6}$$

where $\|\mathbf{J}\|$ is the matrix norm of $\mathbf{G}_J = \mathbf{J}^T \mathbf{J}$, and the Euclidean norm (2-norm) is adopted. Therefore, CN (κ) can be calculated using the square root of the ratio of the maximal and minimal eigenvalues of \mathbf{G}_J , which is expressed as

$$\kappa = \|\mathbf{J}\| \|\mathbf{J}^{-1}\| = \sqrt{\frac{\lambda_{\max}(\mathbf{J}^T \mathbf{J})}{\lambda_{\min}(\mathbf{J}^T \mathbf{J})}}. \tag{7}$$

Matrix \mathbf{G}_J is termed the transfer coefficient matrix, and the components in \mathbf{G}_J , called “transfer coefficients”, represent the velocity amplification factors. The transfer coefficients vary when C_P is changed for different payloads, altering the maximum and minimum of the six eigenvalues of \mathbf{G}_J . Consequently, the CN failed to maintain the optimal value.

2.2. Transfer Coefficients

It is important to derive transfer coefficients to explore how the \mathbf{G}_J eigenvalues change with the C_P location. Partition \mathbf{J} , as $\mathbf{J} = [\mathbf{J}_t \quad \mathbf{J}_r]$ and \mathbf{G}_J , can be divided into four parts:

$$\mathbf{G}_J = \begin{bmatrix} \mathbf{J}_t^T \mathbf{J}_t & \mathbf{J}_t^T \mathbf{J}_r \\ \mathbf{J}_r^T \mathbf{J}_t & \mathbf{J}_r^T \mathbf{J}_r \end{bmatrix}, \tag{8}$$

where \mathbf{J}_t and \mathbf{J}_r are 6×3 matrices that represent the translational and rotational parts, respectively.

For any 3×3 matrix, $\mathbf{A} = \{a_{ij}\}$, the following equation can be derived:

$$\mathbf{A} + \mathbf{R}_{z, \frac{2}{3}\pi} \mathbf{A} \mathbf{R}_{z, \frac{2}{3}\pi}^T + \mathbf{R}_{z, \frac{4}{3}\pi} \mathbf{A} \mathbf{R}_{z, \frac{4}{3}\pi}^T = \frac{3}{2} \begin{bmatrix} a_{11} + a_{22} & a_{12} - a_{21} & \\ a_{21} - a_{12} & a_{11} + a_{22} & \\ & & 2a_{33} \end{bmatrix}. \tag{9}$$

If \mathbf{A} is symmetric, $a_{12} - a_{21} = 0$. Considering this property, the top-left part of \mathbf{G}_J can be obtained as follows:

$$\mathbf{J}_t^T \mathbf{J}_t = \sum_{i=1,2} \left(\mathbf{s}_i \mathbf{s}_i^T + \mathbf{R}_{z, \frac{2}{3}\pi} \mathbf{s}_i \mathbf{s}_i^T \mathbf{R}_{z, \frac{2}{3}\pi}^T + \mathbf{R}_{z, \frac{4}{3}\pi} \mathbf{s}_i \mathbf{s}_i^T \mathbf{R}_{z, \frac{4}{3}\pi}^T \right) = \begin{bmatrix} \eta_{TX} & & \\ & \eta_{TY} & \\ & & \eta_{TZ} \end{bmatrix}, \tag{10}$$

where

$$\begin{cases} \eta_{TX} = \eta_{TY} = \frac{3}{2} (\sin^2 \theta_1 + \sin^2 \theta_2) \\ \eta_{TZ} = 3 (\cos^2 \theta_1 + \cos^2 \theta_2) \end{cases} \tag{11}$$

Notably, $\eta_{TX} + \eta_{TY} + \eta_{TZ} = 6$. Similarly, the rest can be found as

$$\mathbf{J}_r^T \mathbf{J}_r = \sum_{i=1}^6 (\mathbf{p}_i \times \mathbf{s}_i) (\mathbf{p}_i \times \mathbf{s}_i)^T = \begin{bmatrix} \eta_{RX} & & \\ & \eta_{RY} & \\ & & \eta_{RZ} \end{bmatrix}, \tag{12}$$

where

$$\begin{cases} \eta_{RX} = \eta_{RY} = \frac{3}{2} \sum_{i=1,2} [r_{pi}^2 \cos^2 \theta_i + p_{zi}^2 \sin^2 \theta_i - 2r_{pi} p_{zi} \cos \theta_i \sin \theta_i \cos(\omega_{pi} - \varphi_i)] \\ \eta_{RZ} = 3 \sum_{i=1,2} [r_{pi}^2 \sin^2 \theta_i \sin^2(\omega_{pi} - \varphi_i)] \end{cases}, \tag{13}$$

and

$$\mathbf{J}_r^T \mathbf{J}_t = \sum_{i=1}^6 (\mathbf{p}_i \times \mathbf{s}_i) \mathbf{s}_i^T = \begin{bmatrix} \eta_{TXRX} & \eta_{TYRX} & \\ \eta_{TXRY} & \eta_{TYRY} & \\ & & \eta_{TZRZ} \end{bmatrix}, \tag{14}$$

where

$$\begin{cases} \eta_{TXRX} = \eta_{TYRY} = -\frac{1}{2} \eta_{TZRZ} = \frac{3}{2} \sum_{i=1,2} [r_{pi} \cos \theta_i \sin \theta_i \sin(\omega_{pi} - \varphi_i)] \\ \eta_{TXRY} = -\eta_{TYRX} = \frac{3}{2} \sum_{i=1,2} [p_{zi} \sin^2 \theta_i - r_{pi} \cos \theta_i \sin \theta_i \cos(\omega_{pi} - \varphi_i)] \end{cases}. \tag{15}$$

Note that $\eta_{TX}, \eta_{TY}, \eta_{TZ}, \eta_{RX}, \eta_{RY},$ and η_{RZ} characterize the transfer coefficients in each DOF, and $\eta_{TXRX}, \eta_{TYRY}, \eta_{TZRZ}, \eta_{TXRY},$ and η_{TYRX} are the coupling transfer coefficients.

2.2.1. Decoupling Conditions

Coupling is one of the important problems of a multi-DOF shaker. It can cause unexpected responses when the multi-DOF shaker reproduces a desired vibration waveform signal, leading to a reduction in accuracy. The coupling transfer coefficients characterize the coupling of transmissibility between the two DOFs.

Assuming that the BP is fixed to the ground, the dynamic equilibrium of the RSSP is

$$\mathbf{M}_P \ddot{\mathbf{X}}_P + c \mathbf{J}^T \dot{\mathbf{J}} \dot{\mathbf{X}}_P + k \mathbf{J}^T \mathbf{J} \mathbf{X}_P = \mathbf{F}_P \tag{16}$$

where \mathbf{M}_P shows the mass matrix of the MP (including the payload); c and k denote the passive damping and the stiffness of each strut, respectively; and $\mathbf{F}_P = (f_{TX}, f_{TY}, f_{TZ}, t_{RX}, t_{RY}, t_{RZ})^T$ is the excitation force attached to the MP, assuming that \mathbf{M}_P is designed to be diagonal.

If the coupling transfer coefficients become zero, G_J becomes diagonal, and the RSSP becomes decoupled. Equation (16) can be subsequently divided into six equations, representing TX, TY, TZ, RX, RY, and RZ. And the excitation force in one DOF only causes the response in the same DOF, for example, TX to TX, TY to TY, etc., which implies better control performance [36]. Based on this deduction, the decoupling conditions can be given by Equation (15) to make $J_r^T J_t = \mathbf{0}$ as follows:

(i) Decoupling condition 1

$$\eta_{TXRX} = \eta_{TYRY} = -\frac{1}{2}\eta_{TZRZ} = 0 \tag{17}$$

To facilitate discussion, a simplified diagram with strut 1 and 2 is shown in Figure 2, where the blue circles denote the MP and the red arrows denote the struts 1 and 2. A line perpendicular to the symmetry axis $O_B O_P$ is drawn, and the line intersects $O_B O_P$ and $b_1 p_1$ at O_{t1} and q_1 , respectively. To define the angle σ_1 , $\omega_{p1} - \varphi_1 + \sigma_1 = \pi/2$ is employed. The length of $O_{t1} q_1$ is $r_{t1} = r_{p1} \cos \sigma_1 = r_{p1} \sin(\omega_{p1} - \varphi_1)$. Similarly, the angle and length are obtained as $\omega_{p2} - \varphi_2 + \sigma_2 = 3\pi/2$ and $r_{t2} = r_{p2} \cos \sigma_2 = -r_{p2} \sin(\omega_{p2} - \varphi_2)$. Then, the decoupling condition 1 can be derived as follows:

$$r_{t1} \cos \theta_1 \sin \theta_1 = r_{t2} \cos \theta_2 \sin \theta_2. \tag{18}$$

Both groups of RSSP struts lie on a pair of circular hyperboloids formed by rotating struts 1 and 2 around the symmetry axis [37]. Hence, r_{t1} and r_{t2} denote the throat radiuses of the hyperboloids, and O_{t1} and O_{t2} are the two throat centers of the RSSP. In addition, σ_1 and σ_2 define the angle between the throat radius and the MP radius.

(ii) Decoupling condition 2

$$\eta_{TXRY} = -\eta_{TYRX} = 0 \tag{19}$$

Introduce σ_1 and σ_2 and then obtain

$$p_{z1} \sin^2 \theta_1 + p_{z2} \sin^2 \theta_2 = r_{p1} \sin \sigma_1 \cos \theta_1 \sin \theta_1 - r_{p2} \sin \sigma_2 \cos \theta_2 \sin \theta_2. \tag{20}$$

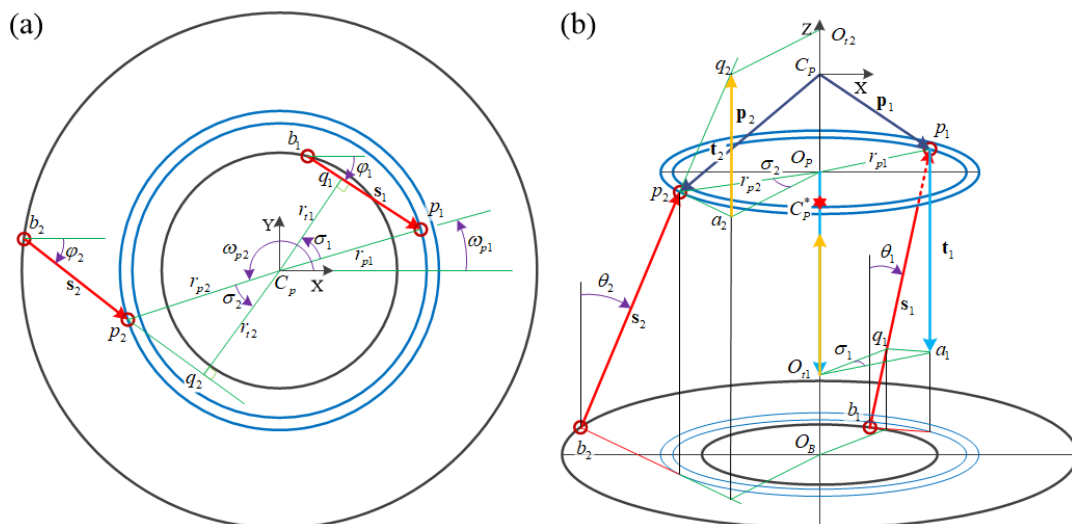


Figure 2. Architecture with struts 1 and 2. (a) Top view; (b) axial view.

2.2.2. Simplification

To simplify the transfer coefficient formulas, let $p_{z1} = p_{z2} = -z_c$ and $\theta_1 = \theta_2 = \theta$ maintain the identical lengths of struts 1 and 2, implying the same throat radiuses from Equation (18), which is expressed as $r_{t1} = r_{t2} = r_t$. The transfer coefficients in G_J are simplified as follows:

$$\begin{cases} \eta_{TX} = \eta_{TY} = 3 \sin^2 \theta \\ \eta_{TZ} = 6 \cos^2 \theta \\ \eta_{RX} = \eta_{RY} = 3 \sin^2 \theta \cdot z_c^2 + 3(r_{p1} \sin \sigma_1 - r_{p2} \sin \sigma_2) \cos \theta \sin \theta \cdot z_c + \frac{3}{2}(r_{p1}^2 + r_{p2}^2) \cos^2 \theta \\ \eta_{RZ} = 6r_t^2 \sin^2 \theta \end{cases} \quad (21)$$

The decoupling condition 1 is met as

$$\eta_{TXRX} = \eta_{TYRY} = -\frac{1}{2}\eta_{TZRZ} = \frac{3}{2} \cos \theta \sin \theta (r_{t1} - r_{t2}) = 0. \quad (22)$$

In addition, decoupling condition 2 is rewritten as

$$\eta_{TXRY} = -\eta_{TYRX} = -3 \sin^2 \theta \cdot z_c - \frac{3}{2}(r_{p1} \sin \sigma_1 - r_{p2} \sin \sigma_2) \cos \theta \sin \theta = 0 \quad (23)$$

which is fulfilled if and only if one of the following equivalents is ensured as follows:

(i) $\sin \theta = 0$

Then, $\theta = 0$, which is a singular pose in which all struts are parallel to the Z-axis; thereby, $\sin \theta = 0$ cannot be satisfied.

(ii) $\sin \theta \neq 0$ and $\sin \theta \cdot z_c + \frac{1}{2}(r_{p1} \sin \sigma_1 - r_{p2} \sin \sigma_2) \cos \theta = 0$

Thus, the decoupling condition is simplified as

$$z_c^* = -\frac{1}{2}(r_{p1} \sin \sigma_1 - r_{p2} \sin \sigma_2) \cot \theta. \quad (24)$$

The following corollaries can be given.

Corollary 1. *The decoupling center, C_p^* , is at the midpoint of the line connecting the two throat centers of the RSSP.*

Proof. As shown in Figure 2b, a vertical line is drawn through p_1 , and the horizontal plane containing $O_{t1}q_1$ at a_1 is intersected. Evidently, triangles $\Delta O_{t1}q_1a_1$ and $\Delta p_1a_1q_1$ share the same side, $|q_1a_1| = r_{p1} \sin \sigma_1$, and then $|p_1a_1| = r_{p1} \sin \sigma_1 \cot \theta$. □

Draw the vectors $\mathbf{t}_1 = (0, 0, -r_{p1} \sin \sigma_1 \cot \theta)^T$ and $\mathbf{t}_2 = (0, 0, r_{p2} \sin \sigma_2 \cot \theta)^T$ in Figure 2b (the blue and yellow arrows). The decoupling center coordinates are $C_p^* = (0, 0, z_c^*)^T = (\mathbf{t}_1 + \mathbf{t}_2)/2$, which lies at the $O_{t1}O_{t2}$ midpoint.

Corollary 2. *The minimum η_{RX} (or η_{RY}) is obtained only if the decoupling condition is satisfied as follows.*

Proof. The following equations are involved in Equation (21).

$$\begin{aligned} d_2 &= 3 \sin^2 \theta \\ d_1 &= 3(r_{p1} \sin \sigma_1 - r_{p2} \sin \sigma_2) \cos \theta \sin \theta \\ d_0 &= \frac{3}{2}(r_{p1}^2 + r_{p2}^2) \cos^2 \theta \end{aligned}$$

It is recognized that the η_{RX} curve is a parabola, which is expressed as

$$\eta_{RX} = \eta_{RY} = d_2 \cdot z_c^2 + d_1 \cdot z_c + d_0.$$

The parabolic vertex is $z_c^* = -d_1 / (2d_2)$, which is the location of the decoupling center, C_p^* , compared with Equation (24). Here, the minimum is

$$\eta_{RX}^* = \eta_{RY}^* = \frac{4d_2d_0 - d_1^2}{4d_2} = \frac{3}{4} \cos^2 \theta \left[r_{p1}^2 (1 + \cos^2 \sigma_1) + r_{p2}^2 (1 + \cos^2 \sigma_2) + 2r_{p1}r_{p2} \sin \sigma_1 \sin \sigma_2 \right] \quad (25)$$

□

3. ICN Condition

3.1. Eigenvalues of the Transfer Coefficient Matrix

The eigenvalues of \mathbf{G}_J should be derived first to obtain the condition for keeping κ constant when C_p moves. From the simplification of the transfer coefficient in Equations (21)–(23), the general form of \mathbf{G}_J can be obtained from the previous analysis as follows:

$$\mathbf{G}_J = \begin{bmatrix} \eta_{TX} & & & & & \\ & \eta_{TX} & & & & \\ & & \eta_{TZ} & & & \\ & & & \eta_{RY} & & \\ \eta_{TXRY} & & & & \eta_{RY} & \\ & & & & & \eta_{RZ} \end{bmatrix} \quad (26)$$

when $z_c \neq z_c^*$, $\eta_{TXRY} \neq 0$, and the characteristic equation is

$$|\lambda \mathbf{E} - \mathbf{G}_J| = \left(\lambda - \eta_{TX} - \frac{\eta_{TXRY}^2}{\lambda - \eta_{RY}} \right)^2 (\lambda - \eta_{RY})^2 (\lambda - \eta_{TZ}) (\lambda - \eta_{RZ}) = 0, \quad (27)$$

where \mathbf{E} is a 6×6 unit matrix, and the eigenvalues are deduced below as

$$\begin{cases} \lambda_{1,2} = \frac{(\eta_{TX} + \eta_{RY}) + \sqrt{(\eta_{TX} - \eta_{RY})^2 + 4\eta_{TXRY}^2}}{2} \\ \lambda_{3,4} = \frac{(\eta_{TX} + \eta_{RY}) - \sqrt{(\eta_{TX} - \eta_{RY})^2 + 4\eta_{TXRY}^2}}{2} \\ \lambda_5 = \eta_{TZ} \\ \lambda_6 = \eta_{RZ} \end{cases} \quad (28)$$

If the decoupling condition is satisfied ($z_c = z_c^*$), the characteristic equation is

$$(\lambda - \eta_{TX})^2 (\lambda - \eta_{RY}^*)^2 (\lambda - \eta_{TZ}) (\lambda - \eta_{RZ}) = 0. \quad (29)$$

The eigenvalues also become

$$\begin{cases} \lambda_{1,2} = \eta_{TX} \\ \lambda_{3,4} = \eta_{RY}^* \\ \lambda_5 = \eta_{TZ} \\ \lambda_6 = \eta_{RZ} \end{cases} \quad (30)$$

3.2. ICN Condition

According to Equation (21), z_c is not included in the formulas for λ_5 and λ_6 . Thus, the CN remains constant when C_p moves along the Z-axis if the following equation is satisfied:

$$\begin{cases} \lambda_{\max} = \max(\lambda_5, \lambda_6) = \max(\eta_{TZ}, \eta_{RZ}) \\ \lambda_{\min} = \min(\lambda_5, \lambda_6) = \min(\eta_{TZ}, \eta_{RZ}) \end{cases} \quad (31)$$

For Equation (28), $\eta_{TXRY}^2 \geq 0$, and the following can be obtained when $\eta_{TX} \geq \eta_{RY}$:

$$\begin{aligned} \lambda_{1,2} &\geq \frac{\eta_{TX} + \eta_{RY}}{2} + \frac{\eta_{TX} - \eta_{RY}}{2} = \eta_{TX} \\ \lambda_{3,4} &\leq \frac{\eta_{TX} + \eta_{RY}}{2} - \frac{\eta_{TX} - \eta_{RY}}{2} = \eta_{RY} \end{aligned}$$

Similarly, when $\eta_{TX} < \eta_{RY}$,

$$\begin{aligned} \lambda_{1,2} &\geq \eta_{RY} \\ \lambda_{3,4} &\leq \eta_{TX} \end{aligned}$$

Therefore, the lower limit of $\lambda_{1,2}$ and the upper limit of $\lambda_{3,4}$ are deduced as

$$\begin{aligned} \lambda_{1,2} &\geq \max(\eta_{TX}, \eta_{RY}) \\ \lambda_{3,4} &\leq \min(\eta_{TX}, \eta_{RY}) \end{aligned} \tag{32}$$

According to Corollary 2, η_{RY} reaches the minimum η_{RY}^* when the decoupling condition is satisfied. In addition, η_{TX} remains constant for z_c ; thus, Equation (31) is satisfied if one of the following conditions is fulfilled as follows:

(i) $\eta_{TZ} \geq \max(\eta_{TX}, \eta_{RY}^*)$ and $\min(\eta_{TX}, \eta_{RY}^*) \geq \eta_{RZ}$

This condition prescribes η_{TZ} and η_{RZ} as the maximum and minimum values, respectively. As expressed in Equation (21), the θ range can be further defined using $\eta_{TZ} \geq \eta_{TX}$. Note that $0 < \theta < \pi/2$. Thus, we obtain

$$0 < \theta \leq \arctan\sqrt{2}. \tag{33}$$

The throat radius is deduced by $\eta_{TX} \geq \eta_{RZ}$:

$$0 < r_t^2 \leq \frac{1}{2}. \tag{34}$$

Considering that $\eta_{TZ} \geq \eta_{RY}^*$ and $\eta_{RY}^* \geq \eta_{RZ}$,

$$r_t^2 \left[(\tan \sigma_1 + \tan \sigma_2)^2 + 4 \right] \leq 8, \tag{35}$$

$$(\tan \sigma_1 + \tan \sigma_2)^2 \geq 8 \tan^2 \theta - 4. \tag{36}$$

ICN condition 1 is defined by Equations (33)–(36), providing the relation of the architecture parameters to make the CN insensitive to z_c , and the analytical form of CN can be found as

$$\kappa = \frac{\cot \theta}{r_t}. \tag{37}$$

For Equations (33) and (36), if $\theta = \arctan\sqrt{2}$, $(\tan \sigma_1 + \tan \sigma_2)^2 = 8 \tan^2 \theta - 4$, and the decoupling condition is satisfied, \mathbf{G}_J becomes a specific form, which is expressed as

$$\mathbf{G}_J = \text{diag}\{\eta_T, \eta_T, \eta_T, \eta_R, \eta_R, \eta_R\},$$

where the transfer coefficients are $\eta_T = 2 = \eta_{TX} = \eta_{TY} = \eta_{TZ}$ and $\eta_R = \eta_{RX} = \eta_{RY} = \eta_{RZ}$. This property is called kinematic isotropy [38]. Furthermore, a particular case of this isotropy is shown when the additional conditions for Equations (34) and (35) are met: $r_t^2 = 1/2$ and $r_t^2 \left[(\tan \sigma_1 + \tan \sigma_2)^2 + 4 \right] = 8$, where the transfer coefficients become identical and equal to 2. The CN reaches the minimum, 1.

(ii) $\eta_{RZ} \geq \max(\eta_{TX}, \eta_{RY}^*)$ and $\min(\eta_{TX}, \eta_{RY}^*) \geq \eta_{TZ}$.

Note that both conditions have the same form; thus, the same derivation of ICN condition 2 is given as

$$\eta_R = \eta_{RX} = \eta_{RY} = \eta_{RZ} \begin{cases} \arctan\sqrt{2} \leq \theta < \frac{\pi}{2} \\ r_t^2 \geq \frac{1}{2} \\ r_t^2 \left[(\tan \sigma_1 + \tan \sigma_2)^2 + 4 \right] \geq 8 \\ (\tan \sigma_1 + \tan \sigma_2)^2 \leq 8 \tan^2 \theta - 4 \end{cases} \tag{38}$$

Herein, the CN is the inverse of Equation (37):

$$\kappa = r_t \tan \theta. \tag{39}$$

This makes an analytical form of the CN possible. Using Equations (37) and (39), the CN can be the demanded value and is guaranteed to be insensitive to the C_P location of z_c by ICN condition 1 or 2. Accordingly, a class of RSSPs with an ICN (ICN-RSSP) can be designed. Note that ICN conditions 1 and 2 provide different requirements for r_t and θ , determining the MP envelope and the total size of a multi-DOF shaker. Therefore, it is necessary to select suitable ICN conditions.

3.3. Area of ICN (AICN)

Given the analytical form of the CN, this section derives the feasible domain of z_c , which is called AICN in this study. The AICN can be calculated by solving the following equation:

$$\begin{aligned} \lambda_{1,2} &= \max(\lambda_5, \lambda_6) \\ \lambda_{3,4} &= \min(\lambda_5, \lambda_6) \end{aligned}$$

Since $\lambda_{1,2}$ and $\lambda_{3,4}$ are quadratic functions of z_c , each equation should have two solutions.

$$z_{c1,2} = -\frac{r_t(\tan \sigma_1 - \tan \sigma_2)}{2 \tan \theta} \pm \frac{1}{2} \sqrt{\left(\frac{2}{\tan^2 \theta} - 1\right) \left[4 - r_t^2 \cdot \frac{4 + (\tan \sigma_1 + \tan \sigma_2)^2}{2}\right]}, \quad (40)$$

$$z_{c3,4} = -\frac{r_t(\tan \sigma_1 - \tan \sigma_2)}{2 \tan \theta} \pm \frac{1}{2} \sqrt{(1 - 2r_t^2) \left[\frac{4 + (\tan \sigma_1 + \tan \sigma_2)^2}{2 \tan^2 \theta} - 4\right]}. \quad (41)$$

Equations (40) and (41) further define the boundaries of the two domains, where the eigenvalues are equal, and AICN represents the intersection of the two domains. Both domains share the same midpoint, which is the decoupling center, C_p^* , in comparison with Equation (24). Accordingly, the AICN can be determined using a domain with a smaller width.

Compare the widths of both domains:

$$|z_{c1} - z_{c2}| = \sqrt{\left(\frac{2}{\tan^2 \theta} - 1\right) \left[4 - r_t^2 \cdot \frac{4 + (\tan \sigma_1 + \tan \sigma_2)^2}{2}\right]}, \quad (42)$$

and

$$|z_{c3} - z_{c4}| = \sqrt{(1 - 2r_t^2) \left[\frac{4 + (\tan \sigma_1 + \tan \sigma_2)^2}{2 \tan^2 \theta} - 4\right]} \quad (43)$$

For simplification, the squares of the widths are employed to analyze the difference in the widths, which is expressed as

$$|z_{c1} - z_{c2}|^2 - |z_{c3} - z_{c4}|^2 = \left[\frac{(\tan \sigma_1 + \tan \sigma_2)^2}{2} - 6\right] \left(r_t^2 - \frac{1}{\tan^2 \theta}\right). \quad (44)$$

For ICN condition 1, considering $\kappa \geq 1$ and Equation (37), $r_t^2 - 1/\tan^2 \theta \leq 0$ is obtained. Similarly, regarding ICN condition 2, $r_t^2 - 1/\tan^2 \theta \geq 0$. To obtain the AICN, $\Delta = (\tan \sigma_1 + \tan \sigma_2)^2$ is calculated first, and then the narrower domain is determined using Equation (44). Subsequently, the appropriate formula can be selected from Equations (40) and (41) to analyze the AICN.

The AICN width, W_{AICN} , partly represents the CN insensitivity. A wider AICN also implies that the CN is less sensitive (i.e., the CN can maintain the desired value over a larger range of z_c). When r_t and θ are determined, Equations (42) and (43) become monotonic

functions of Δ . Thus, only one intersection exists, $\Delta = 12$, according to Equation (44). The maximum value of W_{AICN} is calculated as follows:

$$W_{AICNm} = 2\sqrt{(1 - 2r_t^2) \left(\frac{2}{\tan^2 \theta} - 1 \right)}. \tag{45}$$

4. Design and Numerical Verification

The preceding derivation provides an analytical method for obtaining an ICN and a feasible domain that limits error amplification. To investigate and validate the method, an RSSP was provided for comparison, and a design example was presented and examined.

4.1. RSSP for Comparison

The RSSP for comparison should be decoupled to verify its effectiveness because the design method is based on decoupling conditions. Therefore, an RSSP with kinematic isotropy (KI-RSSP) is represented, referring to [26]. The architecture parameters of the KI-RSSP are listed in Table 1, and the architecture is displayed in Figure 3, where the blue circles and red lines denote the upper-joint distribution circles on the MP and the struts (the end points represent the joints), respectively. For a multi-DOF shaker, the MP envelope determines the payload size to a certain extent; therefore, the MP envelope can be set as a design constraint. The radius of the MP envelope is $r_e = \max(r_{p1}, r_{p2}) = 335$ mm, and the origin point is set at the center of the MP, whereas the BP (black dashed circles) is -300 mm. The decoupling center, C_p^* (black point), of the KI-RSSP is further located at the origin, and the CN is $\kappa_0 = 5.169$.

Table 1. KI-RSSP architecture parameters.

Items	Values
MP radius	$r_{p1} = 250$ mm, $r_{p2} = 335$ mm
BP radius	$r_{b1} = 135.410$ mm, $r_{b2} = 981.950$ mm
Upper-joint distribution angle	$\omega_{p1} = 15^\circ$, $\omega_{p2} = -15^\circ$
Lower-joint distribution angle	$\omega_{b1} = -82.779^\circ$, $\omega_{b2} = 2.789^\circ$
Architecture height	$h = 300$ mm

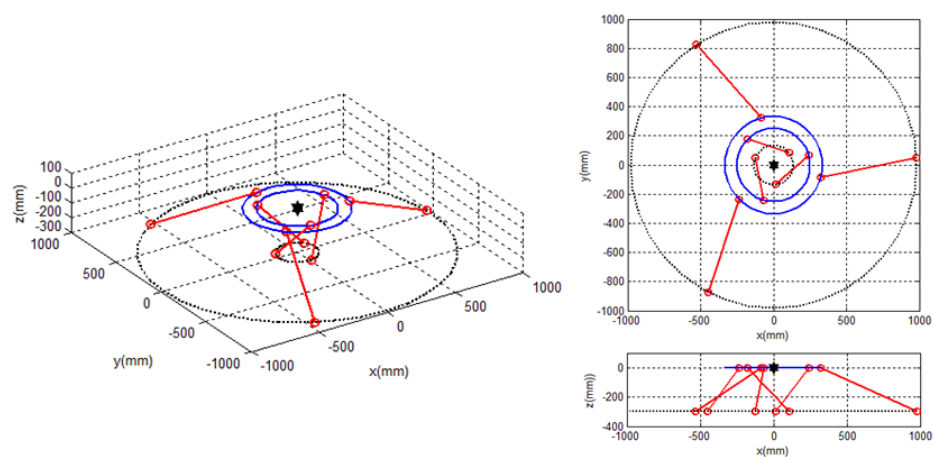


Figure 3. KI-RSSP architecture.

4.2. Design Example of ICN-RSSP

Although a large MP can provide a large installation area for payloads, the MP envelope is limited to decreasing the mass of the moving parts and the energy consumption of the system. Therefore, the MP envelope of the ICN-RSSP should not be larger than that of the KI-RSSP. It should be noted that the MP envelope radius of the KI-RSSP in Table 1

is smaller than 707 mm. Therefore, ICN condition 1 is selected to design the ICN-RSSP according to Equation (34) and is carried out by the following steps:

- (i) Choose $r_t = 250$ mm; to make κ smaller than κ_0 , obtain $\theta = 39^\circ$ via Equations (33) and (37): $\kappa = 4.940$;
- (ii) Calculate the upper and lower limits of Δ via Equations (35) and (36): $1.246 \leq \Delta \leq 124$;
- (iii) Choose σ_1 and σ_2 by designing $\omega_{p1}, \omega_{p2}, \varphi_1,$ and $\varphi_2,$ to make Δ within the limits: let $\omega_{p1} = -\omega_{p2} = 30^\circ$ for simplification, and let $\varphi_1 = -30^\circ$ and $\varphi_2 = 100^\circ$ to obtain $\Delta = 2.006$ and make the MP envelope radius (326.352 mm) smaller than that of the KI-RSSP (335 mm);
- (iv) Involve $r_t, \theta,$ and $\Delta,$ and Equation (44) > 0 can be determined. Therefore, the AICN can be further computed by Equation (41): the midpoint is $z_c^* = 40.404$ mm, and the width is $W_{AICN} = 712.230$ mm.

Table 2 and Figure 4 present the architectural parameters and diagrams, respectively. The decoupling center of the ICN-RSSP can be moved to the required position by adjusting the AICN midpoint in step (iii), if it is necessary to decouple the system to diminish the modeling and controlling complexity.

Table 2. ICN-RSSP architecture parameters.

Items	Values
MP radius	$r_{p1} = 288.675$ mm, $r_{p2} = 326.352$ mm
BP radius	$r_{b1} = 268.740$ mm, $r_{b2} = 517.152$ mm
Upper-joint distribution angle	$\omega_{p1} = 30^\circ, \omega_{p2} = -30^\circ$
Lower-joint distribution angle	$\omega_{b1} = 81.524^\circ, \omega_{b2} = -51.091^\circ$
Architecture height	$h = 300$ mm

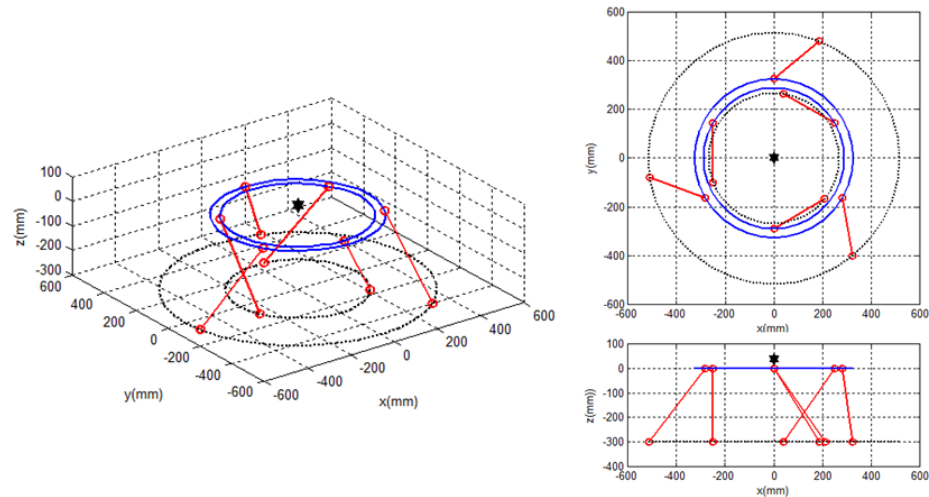


Figure 4. ICN–RSSP architecture.

4.3. Numerical Verification

Numerical analyses of the KI-RSSP and ICN-RSSP are implemented to validate the effectiveness of the method. Figure 5a shows the eigenvalues and transfer coefficients of the KI-RSSP. When $z_c = z_c^*$, the minimum values of $\lambda_{1,2}$ and the maximum values of $\lambda_{3,4}$ coincide with η_{TX} and η_{RY}^* , respectively, because of $\eta_{TX} > \eta_{RY}^*$. From the kinematic isotropy satisfied by the KI-RSSP at the decoupling center, C_p^* , $\eta_{TX} = \eta_{TY} = \eta_{TZ}$, and $\eta_{RX}^* = \eta_{RY}^* = \eta_{RZ}$ can be derived, indicating that the minimum CN occurs at $z_c = z_c^*$. In Figure 5b, there are four intersection points of the eigenvalue curves of the ICN-RSSP that correspond to the four solutions of Equations (40) and (41). The CN of the ICN-RSSP can be further maintained in the range between z_{c2} and z_{c4} for $z_{c2} < z_{c3}$ and $z_{c1} > z_{c4}$. Therefore, the width of the AICN is determined using $W_{AICN} = |z_{c3} - z_{c4}|$. The CN curves of the

KI-RSSP and ICN-RSSP are shown in Figure 6. Compared with the KI-RSSP, the CN of the ICN-RSSP is constant within the AICN and is smaller than the minimum CN of the KI-RSSP. Furthermore, the CN of the ICN-RSSP is smaller than that of the KI-RSSP in the range outside the AICN.

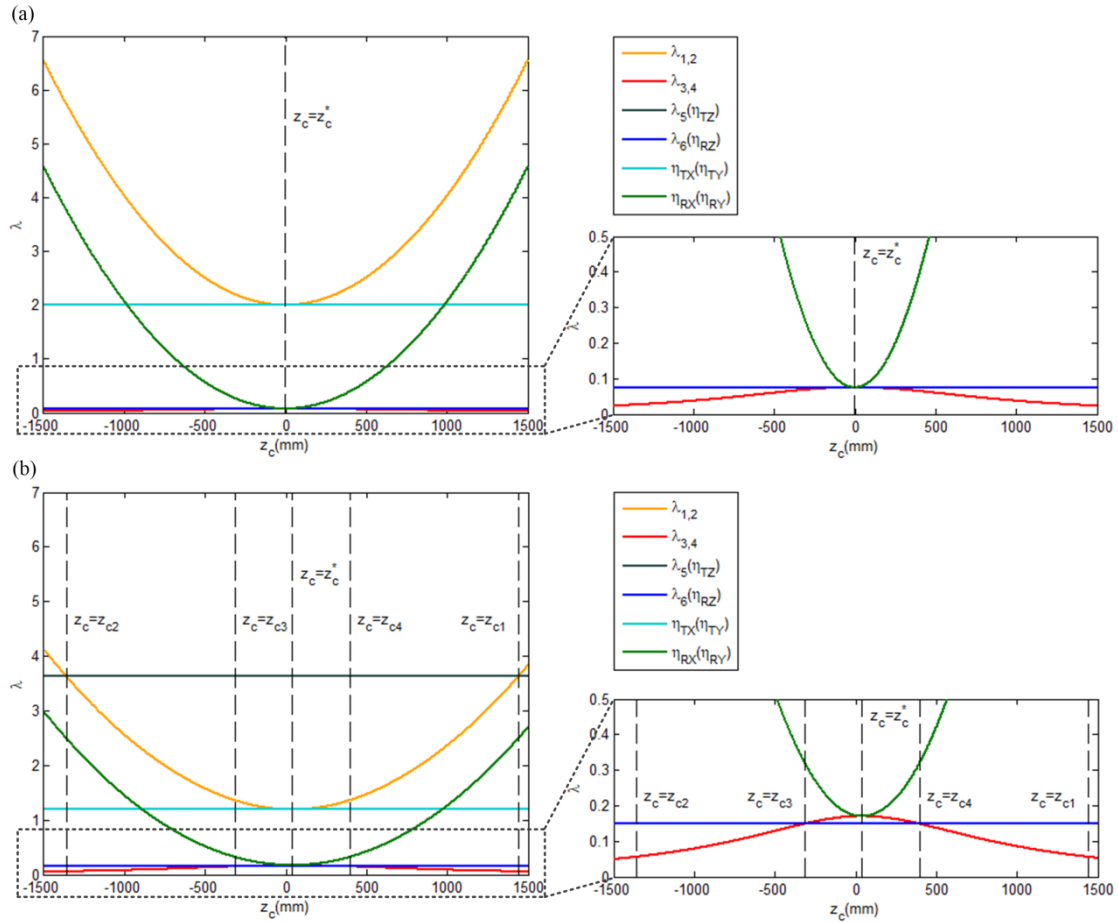


Figure 5. Eigenvalue and transfer coefficient curves: (a) KI-RSSP; (b) ICN-RSSP.

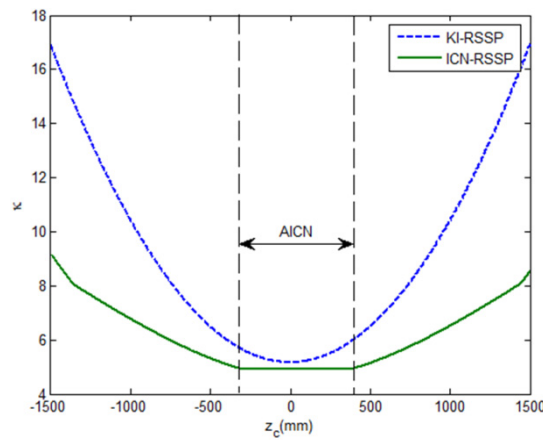


Figure 6. CN curves.

In real situations, C_P is not set exactly on the Z axis of the multi-DOF shaker, causing the CN to change. The C_P deviations from the Z axis are assumed to be x_c and y_c , and the rate of change can be defined as

$$\zeta_c = \frac{|\kappa_c - \kappa_0|}{\kappa_0} \times 100\%, \tag{46}$$

where κ_c is the CN at $(x_c, y_c, z_c)^T$, and κ_0 is the CN at the decoupling center. Several spatial scatter points with a constant ζ_c can be obtained by searching and calculating with the appropriate steps. A closed surface is further attained by splicing these scattered points, which is called the iso- ζ_c surface in this study, to define the space with low CN sensitivity. The space is equivalent to the AICN when $\zeta_c = 0$. Let $\zeta_c = 1\%$, and the iso- ζ_c surfaces are plotted in Figure 7. The shape of the KI-RSSP is approximately spherical, while that of the ICN-RSSP approximates a cocoon upright along the Z axis. By computing the volume of each space by integration, the ICN-RSSP is 16.050 times the KI-RSSP, indicating that the CN of the ICN-RSSP can increase less than 1% in a larger space. These analysis results demonstrate that the given method can design and minimize the CN and expand the low-sensitive space of the CN. Meanwhile, the MP envelope is not increased.

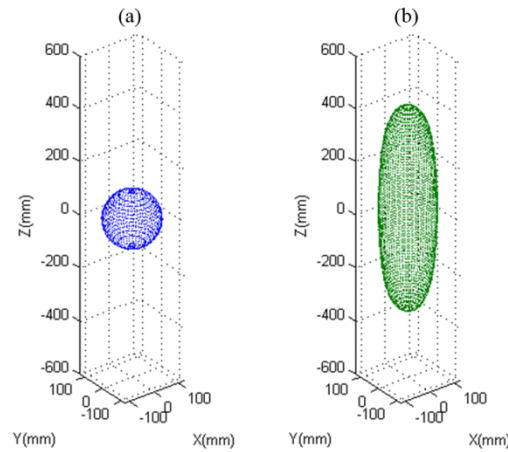


Figure 7. Iso- ζ_c surfaces ($\zeta_c = 1\%$). (a) KI-RSSP; (b) ICN-RSSP.

To demonstrate the effectiveness of reducing the error amplification, let \mathbf{e}_L and \mathbf{e}_P be the actuator and MP error vectors, respectively, and make the modulus of \mathbf{e}_L constant 1:

$$\mathbf{e}_L^T \mathbf{e}_L = 1. \tag{47}$$

It is a six-dimensional sphere, and constant 1 denotes the energy of the actuator errors. From Equations (1) and (47), it can be transformed into a six-dimensional hyper-ellipsoid equation:

$$\mathbf{e}_P^T \mathbf{J}^T \mathbf{J} \mathbf{e}_P = 1. \tag{48}$$

Equation (48) can be expanded by integrating Equation (26). To facilitate discussion, the projections of the hyper-ellipsoid on each 2-DOF plane are displayed in Figure 8a,b, when z_c varies from -1500 mm to 1500 mm. The semi-major axis of each ellipse describes the maximum error in each diagram, and the maximum error occurs in TX-RY. As C_P moves away from the decoupling center, the TX error intensifies because of the coupling between TX and RY. Comparing the TX-RY diagrams in Figure 8c,d, the maximum TX and RY errors of the ICN-RSSP are 69.80% and 66.85%, respectively, of the KI-RSSP. The hyper-ellipsoid analysis results demonstrate that the proposed method can reduce the transfer error amplification of the multi-DOF shaker and maintain this advantage in a larger space for the manipulation center, which is meaningful for multi-DOF shakers to improve motion accuracy and control performance [21].

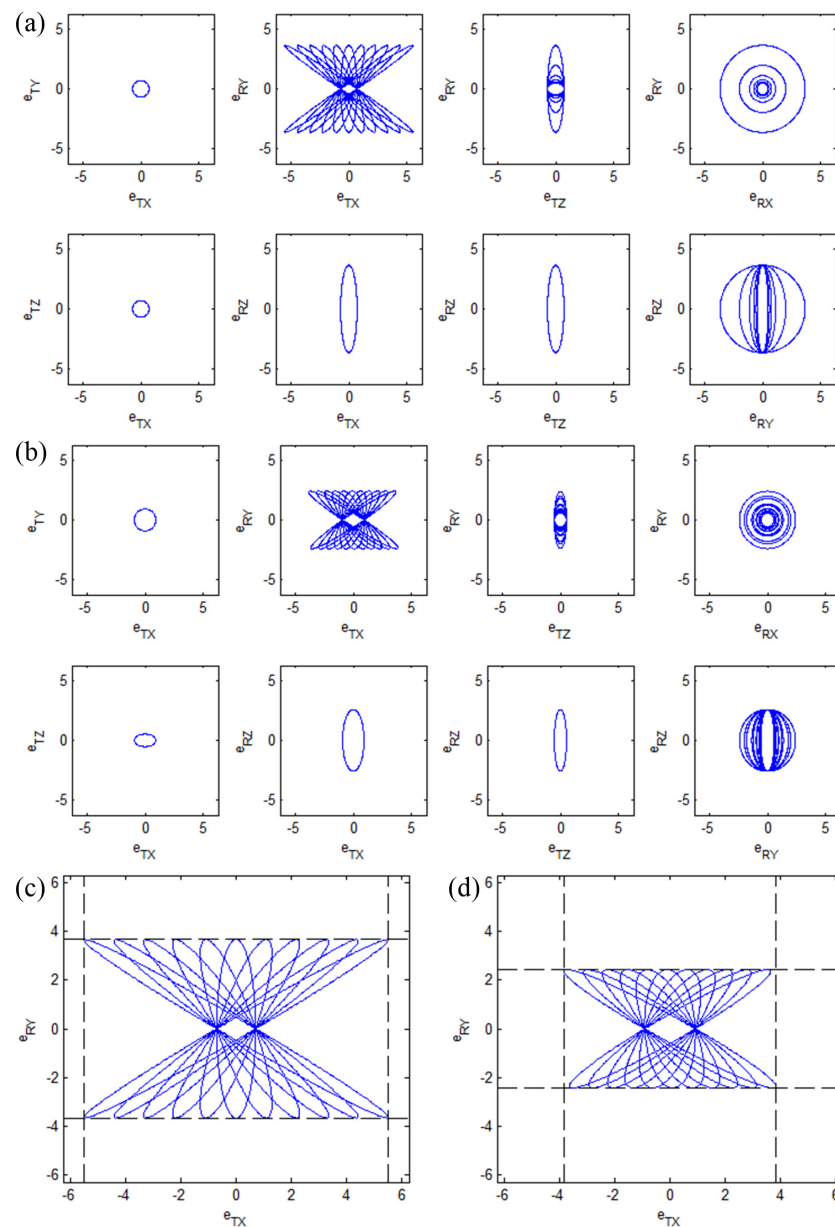


Figure 8. Projection of hyper-ellipsoid. (a) KI-RSSP; (b) ICN-RSSP; (c) TX-RY diagram of KI-RSSP; (d) TX-RY diagram of ICN-RSSP.

5. Development and Experiment of the Multi-DOF Shaker

5.1. Development of the Multi-DOF Shaker

A multi-DOF shaker prototype is developed based on the architecture parameters of the ICN-RSSP listed in Table 2. The six struts are configured in line with the architecture displayed in Figure 9. Each strut contains an actuator, two hook joints (the lower and the upper joints), and a rod connecting the two joints. The actuator is based on the voice coil motor. The fixed part of the actuator is fixed to the ground, and the moving part is driven by the actuation force and can only move along the axis of the fixed part. The lower joint is a 3-DOF hook joint, connecting the moving part of the actuator and the lower end of the rod, while the upper joint is a 2-DOF hook, connecting the upper end of the rod and the MP. Therefore, the multi-DOF shaker includes 13 moving bodies, six translational joints, six spherical joints, and six universal joints. And the number of DOFs is six, equal to the number of actuators, which implies that the multi-DOF shaker can be fully controlled by the six actuators.

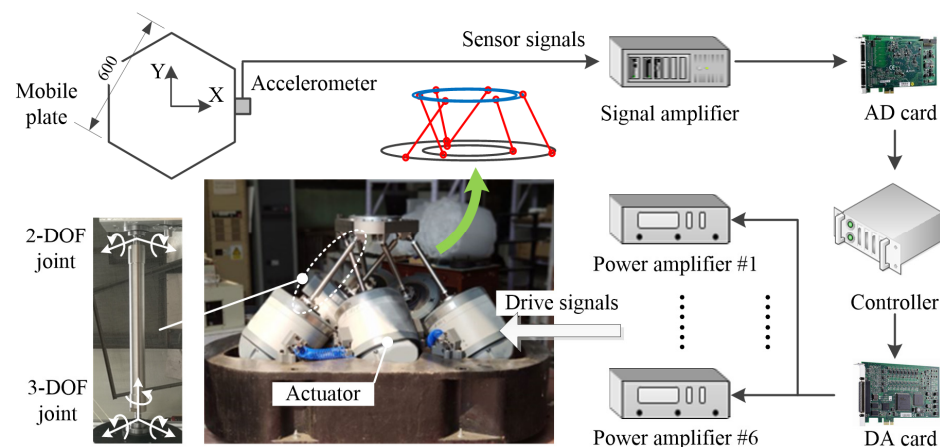


Figure 9. System development of the multi-DOF shaker.

The MP is designed as a regular hexagon with a diameter of 600 mm, and the X and Y axes are shown in Figure 9. Maintaining the same strut length allows for the same design of the actuators and joints, reducing the structural design complexity.

Accelerometers are attached to the MP to measure its 6-DOF acceleration of the MP (or payload) to ensure the accuracy of the desired vibration waveform reproduction. A real-time controller is adopted to process the sensor signals via the AD card and the signal amplifier and produce the drive signals through the DA card and the power amplifiers to control the multi-DOF shaker.

5.2. Experiment Results

A vibration excitation experiment was conducted to validate the effectiveness of the multi-DOF shaker for vibration waveform reproduction. The total mass of the moving parts for the vibration excitation experiment, including the MP and payload, was 51.08 kg. The experimental condition was the swept frequency sinusoidal vibration in RX, RY, and RZ, with the desired angular velocity amplitude of $5^\circ/\text{s}$, because the precise payloads were more sensitive to rotation errors. The frequency range of the experiment was 5–200 Hz, and the sweep rate was 1 Hz/s. The controller was further developed and presented in [39] by using adaptive disturbance cancellation (ADC), which is a typical time-domain control method for sinusoidal signals.

To evaluate the accuracy, the amplitude ratio and phase difference in the RX, RY, and RZ measured signals in the frequency domain of 5–200 Hz were calculated, and the results are shown in Figure 10. The left and right columns show the amplitude–frequency and phase–frequency curves, respectively. Here, the amplitude and phase errors are smaller than 10% and 10° in the frequency band, except for 104 Hz (111.63%, -2.55°) and 111 Hz (83.39%, -3.66°) in RZ, respectively, which were caused by the local vibration modes. The waveforms at 104 and 111 Hz are displayed in Figure 11a,b, where the blue lines and red dashed lines denote the measured signal and the desired signals, respectively. The real-time sweeping frequency was recorded along with time; thus, time can be replaced by frequency as the horizontal axis to directly exhibit the waveform at each frequency. The measured signal agreed well with the desired signal, although there were some amplitude errors and high-frequency noise. The results demonstrated the effectiveness of the method for obtaining a highly accurate multi-DOF shaker.

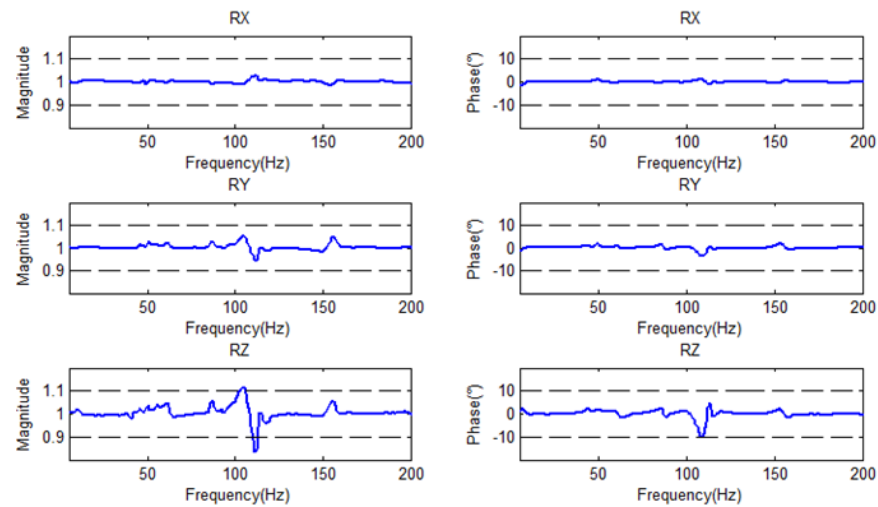


Figure 10. Error analysis of the experiment results.

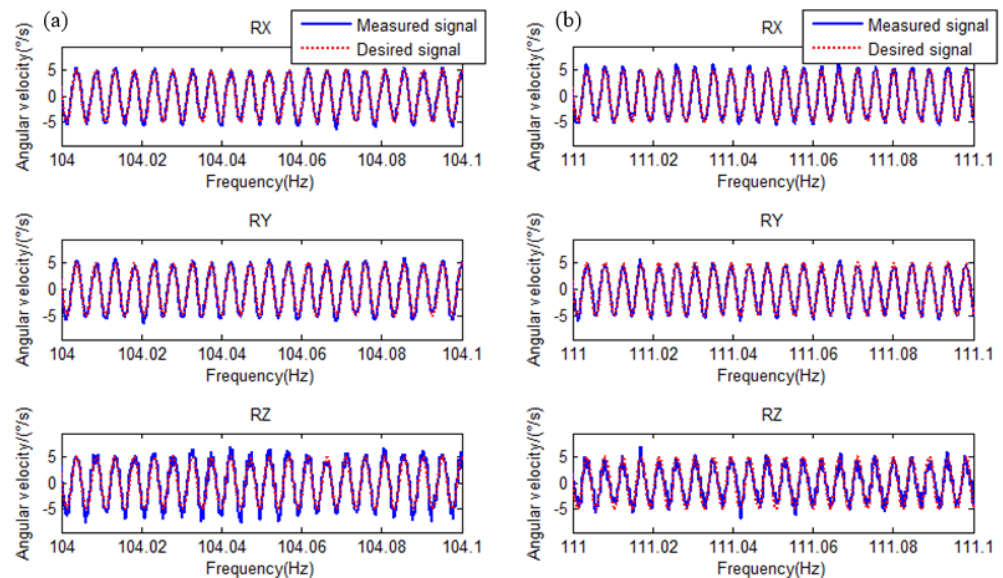


Figure 11. Waveforms at (a) 104 Hz and (b) 111 Hz.

6. Conclusions

This study provided a new analytical method to design a class of RSSPs with ICN and used the method for a multi-DOF shaker design to reduce its motion error. Based on RSSP rotational symmetry, an analytical relationship between the architecture parameters and transfer coefficients of \mathbf{G}_J was established, and the decoupling conditions were deduced. The transfer coefficients were simplified using the decoupling conditions and the assumption of the iso-length struts. Based on this simplification, the eigenvalues of the \mathbf{G}_J were discussed, and the ICN conditions can be derived. Correspondingly, an analytical form of the CN was provided. Subsequently, the AICN concept was proposed, and its design formula was determined. A design example and numerical analysis were carried out to validate the effectiveness of the method. The numerical calculation results verified the effectiveness of the method at minimizing the CN and improving its insensitivity. Finally, a multi-DOF shaker was developed based on the design example, and the multi-DOF vibration excitation experimental results showed small vibration waveform errors. In addition, this method can be used to design other parallel robots that require high-precision motion control, such as a motion simulator [40], parallel machine tools [41] and precise positioning and pointing devices [42].

Author Contributions: Conceptualization, C.L. and W.L.; methodology, C.L. and H.H.; software, Y.Z.; theoretical analysis and validation, C.L. and Y.Z.; investigation, C.L.; writing—original draft preparation, C.L.; writing—review and editing, C.L., W.L. and Y.Z.; supervision, W.L. and H.H.; project administration, H.H.; funding acquisition, W.L. All authors have read and agreed to the published version of the manuscript.

Funding: This research work was supported by the National Key Research and Development Program of China (grant no. 2021YFA1003503).

Data Availability Statement: Not applicable.

Conflicts of Interest: The authors declare no conflict of interest.

Abbreviations

The following abbreviations are used in this manuscript:

DOF	Degree-of-freedom
CN	Condition number
ICN	Insensitive CN
AICN	Area of the ICN
SSP	Standard Stewart platform
GSP	Generalized Stewart platform
RSSP	Rotationally symmetric Stewart platform
KI-RSSP	RSSP with kinematic isotropy
ICN-RSSP	RSSP with an ICN
MP	Mobile plate
BP	Base plate
ADC	Adaptive disturbance cancellation

References

- Hatamleh, K.S.; Ma, O.; Flores-Abad, A.; Xie, P. Development of a Special Inertial Measurement Unit for UAV Applications. *J. Dyn. Syst. Meas. Control.* **2013**, *135*, 011003. [[CrossRef](#)]
- Zhao, S.; Chen, L.; Guan, N.; Zhou, Y.; Zhang, D.; Shu, X.; Liu, C. Angle Error from Vibrating in Tri-Axial Interferometric Fiber Optic Gyroscopes and the Evaluation with Dual-Laser Doppler Vibrometers. *Opt. Fiber Technol.* **2020**, *54*, 102071. [[CrossRef](#)]
- Zhou, J.; Li, Y.; Chen, J.; Nian, L.; Zhang, H. Research on Six Degrees of Freedom Compound Control Technology for Improving Photoelectric Pod Pointing Accuracy. *Opt. Rev.* **2017**, *24*, 579–589. [[CrossRef](#)]
- Capriglione, D.; Carratù, M.; Catelani, M.; Ciani, L.; Patrizi, G.; Singuaroli, R.; Pietrosanto, A.; Sommella, P. Development of a Test Plan and a Testbed for Performance Analysis of MEMS-Based IMUs under Vibration Conditions. *Meas. J. Int. Meas. Confed.* **2020**, *158*, 107734. [[CrossRef](#)]
- Tao, Y.; Rui, X.; Yang, F.; Zhang, J. Study on the Dynamics of IMU Isolation System Based on Transfer Matrix Method for Multibody Systems. In Proceedings of the ASME 2018 International Design Engineering Technical Conferences and Computers and Information in Engineering Conference, Quebec City, QC, Canada, 26–29 August 2018; Volume 6, pp. 1–8. [[CrossRef](#)]
- Ma, L.; Jiang, X.; Dong, L.; Cao, J.; Jin, Y.; Shi, G. Vibration Effects Rectification of IMU Attitude Based on Gradient Descent Algorithm. In Proceedings of the 2017 IEEE International Conference on Real-time Computing and Robotics (RCAR), Okinawa, Japan, 14–18 July 2017; Volume 2017, pp. 167–171.
- Zaiss, C.; Spiewak, S. Vibration Rectification and Thermal Disturbances in Ultra Precision Inertial Sensors. In Proceedings of the ASME 2011 International Mechanical Engineering Congress and Exposition, Denver, CO, USA, 11–17 November 2011; Volume 11, pp. 531–538. [[CrossRef](#)]
- de Pasquale, G.; Somà, A. Reliability Testing Procedure for MEMS IMUs Applied to Vibrating Environments. *Sensors* **2010**, *10*, 456–474. [[CrossRef](#)]
- Capriglione, D.; Carratu, M.; Catelani, M.; Ciani, L.; Patrizi, G.; Pietrosanto, A.; Sommella, P. Experimental Analysis of Filtering Algorithms for IMU-Based Applications under Vibrations. *IEEE Trans. Instrum. Meas.* **2021**, *70*, 3507410. [[CrossRef](#)]
- Gregory, D.; Bitsie, F.; Smallwood, D.O. *Comparison of the Response of a Simple Structure to Single Axis and Multiple Axis Random Vibration Inputs*; Sandia National Laboratory: Albuquerque, NM, USA, 2008; p. 87185.
- He, G.; Chen, H.; Sun, J. Dynamic Responses of Structures under Multiaxial and Uniaxial Random Excitations. *Zhendong Yu Chongji/J. Vib. Shock* **2017**, *36*, 194–201. [[CrossRef](#)]
- Ernst, M.; Habtour, E.; Dasgupta, A.; Pohland, M.; Robeson, M.; Paulus, M. Comparison of Electronic Component Durability under Uniaxial and Multiaxial Random Vibrations. *J. Electron. Packag. Trans.* **2015**, *137*, 011009. [[CrossRef](#)]
- Chen, M.; Wilson, D. The New Triaxial Shock and Vibration Test System at Hill Air Force Base. *J. IEST* **1998**, *41*, 27–32. [[CrossRef](#)]

14. Stewart, D. A Platform with Six Degrees of Freedom. *Proc. Inst. Mech. Eng.* **1965**, *180*, 371–386. [[CrossRef](#)]
15. Furqan, M.; Suhaib, M.; Ahmad, N. Studies on Stewart Platform Manipulator: A Review. *J. Mech. Sci. Technol.* **2017**, *31*, 4459–4470. [[CrossRef](#)]
16. Zhao, Q.; Guo, J.; Yu, D.; Hong, J.; Liu, Z. A Novel Approach of Input Tolerance Design for Parallel Mechanisms Using the Level Set Method. *Proc. Inst. Mech. Eng. Part B J. Eng. Manuf.* **2020**, *234*, 371–381. [[CrossRef](#)]
17. Li, F.; Zeng, Q.; Ehmman, K.F.; Cao, J.; Li, T. A Calibration Method for Overconstrained Spatial Translational Parallel Manipulators. *Robot. Comput. Integr. Manuf.* **2019**, *57*, 241–254. [[CrossRef](#)]
18. Karimi, D.; Nategh, M.J. Contour Maps for Developing Optimal Toolpath and Workpiece Setup in Hexapod Machine Tools by Considering the Kinematics Nonlinearity. *Proc. Inst. Mech. Eng. Part B J. Eng. Manuf.* **2016**, *230*, 1572–1583. [[CrossRef](#)]
19. Merlet, J.P. Jacobian, Manipulability, Condition Number, and Accuracy of Parallel Robots. *J. Mech. Des.* **2006**, *128*, 199–206. [[CrossRef](#)]
20. Pulloquina, J.L.; Mata, V.; Valera, Á.; Zamora-Ortiz, P.; Díaz-Rodríguez, M.; Zambrano, I. Experimental Analysis of Type II Singularities and Assembly Change Points in a 3UPS+RPU Parallel Robot. *Mech. Mach. Theory* **2021**, *158*, 104242. [[CrossRef](#)]
21. Pittens, K.H.; Podhorodeski, R.P. A Family of Stewart Platforms with Optimal Dexterity. *J. Robot. Syst.* **1993**, *10*, 463–479. [[CrossRef](#)]
22. Mehta, V.K.; Dasgupta, B. A General Approach for Optimal Kinematic Design of 6-DOF Parallel Manipulators. *Sadhana Acad. Proc. Eng. Sci.* **2011**, *36*, 977–994. [[CrossRef](#)]
23. Peng, L.; Tong, Z.; Li, C.; Jiang, H.; He, J. Optimal Design of an Orthogonal Generalized Parallel Manipulator Based on Swarm Particle Optimization Algorithm. In Proceedings of the Intelligent Robotics and Applications: 10th International Conference, ICIRA 2017, Wuhan, China, 16–18 August 2017; pp. 334–345. [[CrossRef](#)]
24. McInroy, J.E.; Obrien, J.F.; Allais, A.A. Designing Micromanipulation Systems for Decoupled Dynamics and Control. *IEEE/ASME Trans. Mechatron.* **2015**, *20*, 553–563. [[CrossRef](#)]
25. Klein, C.A.; Miklos, T.A. Spatial Robotic Isotropy. *Int. J. Rob. Res.* **1991**, *10*, 426–437. [[CrossRef](#)]
26. Yi, Y.; McInroy, J.E.; Jafari, F. Generating Classes of Orthogonal Gough-Stewart Platforms. In Proceedings of the IEEE International Conference on Robotics and Automation, New Orleans, LA, USA, 26 April–1 May 2004; Volume 2004, pp. 4969–4974. [[CrossRef](#)]
27. Jiang, H.Z.; Tong, Z.Z.; He, J.F. Dynamic Isotropic Design of a Class of Gough-Stewart Parallel Manipulators Lying on a Circular Hyperboloid of One Sheet. *Mech. Mach. Theory* **2011**, *46*, 358–374. [[CrossRef](#)]
28. Ben-horin, R.; Shoham, M.; Dayan, J. On the Isotropic Configurations of Six Degrees-of-Freedom Parallel Manipulators. *IFAC Proc. Vol.* **1997**, *30*, 235–238. [[CrossRef](#)]
29. Li, W.; Angeles, J. The Design for Isotropy of a Class of Six-Dof Parallel-Kinematics Machines. *Mech. Mach. Theory* **2018**, *126*, 34–48. [[CrossRef](#)]
30. Abdel-Malek, K. Criterion for the Locality of a Manipulator Arm with Respect to an Operating Point. *Proc. Inst. Mech. Eng. Part B J. Eng. Manuf.* **1996**, *210*, 385–394. [[CrossRef](#)]
31. Legnani, G.; Tosi, D.; Fassi, I.; Giberti, H.; Cinquemani, S. The “Point of Isotropy” and Other Properties of Serial and Parallel Manipulators. *Mech. Mach. Theory* **2010**, *45*, 1407–1423. [[CrossRef](#)]
32. Zlatkin, Y.M.; Kalnoguz, A.N.; Voronchenko, V.G.; Lykholit, N.I.; Vakhlov, A.Y.; Sladky, A.M.; Slyusar, V.M. Laser SINS for Cyclone-4 Launch Vehicle. *Gyroscopy Navig.* **2013**, *4*, 156–163. [[CrossRef](#)]
33. Wang, L.; Wu, W.; Pan, X. Dynamic Error Compensation and Parameter Optimization for RLG SINS in Vibration Environments. 2017 24th Saint Petersburg. In Proceedings of the 2017 24th Saint Petersburg International Conference on Integrated Navigation Systems (ICINS), St. Petersburg, Russia, 29–31 May 2017. [[CrossRef](#)]
34. Salisbury, J.K.; Craig, J.J. Articulated Hands: Force Control and Kinematic Issues. *Int. J. Rob. Res.* **1982**, *1*, 4–17. [[CrossRef](#)]
35. McInroy, J.E.; Jafari, F. Finding Symmetric Orthogonal Gough-Stewart Platforms. *IEEE Trans. Robot.* **2006**, *22*, 880–889. [[CrossRef](#)]
36. Yang, C.; Qu, Z.; Han, J. Decoupled-Space Control and Experimental Evaluation of Spatial Electrohydraulic Robotic Manipulators Using Singular Value Decomposition Algorithms. *IEEE Trans. Ind. Electron.* **2014**, *61*, 3427–3438. [[CrossRef](#)]
37. Jiang, H.Z.; He, J.F.; Tong, Z.Z.; Wang, W. Dynamic Isotropic Design for Modified Gough-Stewart Platforms Lying on a Pair of Circular Hyperboloids. *Mech. Mach. Theory* **2011**, *46*, 1301–1315. [[CrossRef](#)]
38. Bandyopadhyay, S.; Ghosal, A. An Algebraic Formulation of Kinematic Isotropy and Design of Isotropic 6-6 Stewart Platform Manipulators. *Mech. Mach. Theory* **2008**, *43*, 591–616. [[CrossRef](#)]
39. Zheng, Y.; Zhou, Z.; Huang, H. A Precise Identification and Control Method for the 6D Micro-Vibration Exciting System. *J. Vib. Eng. Technol.* **2021**, *9*, 1511–1531. [[CrossRef](#)]
40. Tong, Z.; Gosselin, C.; Jiang, H. Dynamic Decoupling Analysis and Experiment Based on a Class of Modified Gough-Stewart Parallel Manipulators with Line Orthogonality. *Mech. Mach. Theory* **2020**, *143*, 103636. [[CrossRef](#)]
41. Guo, J.; Wang, D.; Fan, R.; Chen, W.; Zhao, G. Kinematic Calibration and Error Compensation of a Hexaglide Parallel Manipulator. *Proc. Inst. Mech. Eng. Part B J. Eng. Manuf.* **2019**, *233*, 215–225. [[CrossRef](#)]
42. Yun, H.; Liu, L.; Li, Q.; Li, W.; Tang, L. Development of an Isotropic Stewart Platform for Telescope Secondary Mirror. *Mech. Syst. Signal Process.* **2019**, *127*, 328–344. [[CrossRef](#)]

Disclaimer/Publisher’s Note: The statements, opinions and data contained in all publications are solely those of the individual author(s) and contributor(s) and not of MDPI and/or the editor(s). MDPI and/or the editor(s) disclaim responsibility for any injury to people or property resulting from any ideas, methods, instructions or products referred to in the content.